Frequency-difference electrical impedance tomography (fdEIT): algorithm development and feasibility study

Jin Keun Seo[1]**, Jeehyun Lee**[1]**, Sung Wan Kim**[1]**, Habib Zribi**[1]
and Eung Je Woo[2]

[1] Department of Mathematics, Yonsei University, Korea
[2] College of Electronics and Information, Kyung Hee University, Korea

E-mail: ejwoo@khu.ac.kr

Abstract
Frequency-difference electrical impedance tomography (fdEIT) has been proposed to deal with technical difficulties of a conventional static EIT imaging method caused by unknown boundary geometry, uncertainty in electrode positions and other systematic measurement artifacts. In fdEIT, we try to produce images showing changes of a complex conductivity distribution with respect to frequency. Simultaneously injecting currents with at least two frequencies, we find differences of measured boundary voltages between those frequencies. In most previous studies, real parts of frequency-difference voltage data were used to reconstruct conductivity changes and imaginary parts to reconstruct permittivity changes. This conventional approach neglects the interplay of conductivity and permittivity upon measured boundary voltage data. In this paper, we propose an improved fdEIT image reconstruction algorithm that properly handles the interaction. It uses weighted frequency differences of complex voltage data and a complex sensitivity matrix to reconstruct frequency-difference images of complex conductivity distributions. We found that there are two major sources of image contrast in fdEIT. The first is a contrast in complex conductivity values between an anomaly and background. The second is a frequency dependence of a complex conductivity distribution to be imaged. We note that even for the case where conductivity and permittivity do not change with frequency, the fdEIT algorithm may show a contrast in frequency-difference images of complex conductivity distributions. On the other hand, even if conductivity and permittivity values significantly change with frequency, there is an example where we cannot find any contrast.

The performance of the proposed method is demonstrated by using computer simulations to validate its feasibility in future experimental studies.

(Some figures in this article are in colour only in the electronic version)

1. Introduction

In electrical impedance tomography (EIT), we inject currents into an imaging object such as the human body through surface electrodes so that induced internal current pathways are dictated by its complex conductivity distribution to be imaged. In this paper, the complex conductivity means $\sigma + i\omega\varepsilon$ in S m^{-1} where σ, ω and ε are the conductivity, angular frequency and permittivity, respectively. Local change of an internal complex conductivity value results in a distortion of the current pathway whose effect is conveyed to boundary voltage data which take complex values. EIT uses these measured boundary voltage data to reconstruct images of the complex conductivity distribution inside the imaging object (Webster 1990, Metherall *et al* 1996, Cheney *et al* 1999, Saulnier *et al* 2001, Holder 2005).

In a static EIT imaging method, we may construct a forward model of the imaging object with a presumed complex conductivity distribution. Injecting the same currents into the model, boundary voltages are computed to numerically simulate measured data. Since the initially guessed complex conductivity distribution of the model is in general different from the unknown complex conductivity distribution of the object, there exist some differences between measured and computed voltages. Most static EIT imaging methods are based on a minimization technique where a sum of these voltage differences is minimized by adjusting the complex conductivity distribution of the model (Yorkey *et al* 1987, Cheney *et al* 1990, Woo *et al* 1993, Lionheart *et al* 2005, Adler and Lionheart 2006). Other methods may include the layer-stripping (Cheney *et al* 1991) and d-bar (Isaacson *et al* 2004) algorithms.

In order for a static EIT image reconstruction algorithm to be reliable, we should construct a forward model that mimics every aspect of the imaging object except the internal complex conductivity distribution. This requires knowledge of the boundary geometry, electrode positions and other sources of systematic artifacts in measured data. However, in practice, it is difficult to obtain such information with a reasonable accuracy and cost. Since static EIT imaging is sensitive to these errors, it has a limited applicability so far.

New methods are desirable to overcome these difficulties. One way is to adopt a time-difference imaging method where any difference of an internal complex conductivity distribution between two time instances is imaged (Metherall *et al* 1996, Holder 2005, Oh *et al* 2008). Even though numerous time-difference EIT (tdEIT) methods have been applied to image lung functions, stomach emptying, brain functions and others, there are cases where time-referenced data are not available. For example, in all applications of EIT for tumor imaging including breast tumor, time-referenced data do not exist at the time of imaging since the patient either has tumor or not at that time. Stroke-type detection using EIT is another example. In those cases, static EIT imaging has been tried but reconstructed images suffered from the above-mentioned technical difficulties.

We note that complex conductivity spectra of numerous biological tissues show frequency-dependent changes (Gedded and Baker 1967, Gabriel *et al* 1967, Grimnes and Martinsen 2000,

Oh *et al* 2008). This indicates that we can view a complex conductivity distribution inside an imaging object as a function of frequency. Based on this observation, there have been attempts to perform frequency-difference image reconstructions (Griffiths 1987, Scalfe *et al* 1994, Schlappa *et al* 2000, Yerworth *et al* 2003). However, there has been not much study on its theory and reconstruction algorithm as well as experimental results.

In this paper, we pay attention to frequency-difference EIT (fdEIT) where we inject currents with at least two different frequencies. Utilizing differences of measured boundary voltages between chosen frequencies, we try to alleviate undesirable effects of modeling errors. By investigating the sensitivity of frequency-difference voltage data to a change in a complex conductivity distribution, we will propose an improved frequency-difference image reconstruction algorithm. We will test its performance through numerical simulations assuming a 16-channel multi-frequency EIT system with a frequency range of 10 Hz to 500 kHz (Oh *et al* 2007a, 2007b).

For image reconstructions of complex conductivity distributions, most previous studies have used real parts of complex voltage data to reconstruct conductivity images and their imaginary parts to reconstruct permittivity images. This traditional approach neglects the interplay of conductivity and permittivity values upon measured complex voltage data. It becomes inappropriate especially for a frequency above 1 kHz, for example, where $\omega\epsilon$ values of biological tissues get bigger to be comparable with their σ values. In this paper, we suggest using weighted frequency differences of complex voltage data together with a complex sensitivity matrix to properly handle the interaction.

We will discuss that there are two major sources of image contrast in fdEIT. The first is a contrast in complex conductivity values between an anomaly and background. The second is a frequency dependence of a complex conductivity distribution to be imaged. Since these two are interrelated, there is an example where we cannot see any contrast in reconstructed frequency-difference images even though a true complex conductivity distribution has a strong frequency dependence. On the other hand, fdEIT may visualize an anomaly as long as its complex conductivity differs from that of the background, without requiring any frequency dependence. The performance of the proposed method will be demonstrated by using computer simulations to validate its feasibility in future experimental studies.

2. Methods

2.1. Problem formulation

Let an imaging object occupy a two- or three-dimensional region Ω bounded by its surface $\partial\Omega$. Electrodes $\mathcal{E}_j$ for $j = 1, \ldots, n$ are attached on the boundary $\partial\Omega$. We inject a sinusoidal current with its magnitude I and angular frequency ω through a chosen pair of electrodes and measure boundary voltages between other pairs of electrodes. The resulting time-harmonic voltage u_ω in Ω is governed by

$$\begin{cases} \nabla \cdot ((\sigma(\mathbf{r}, \omega) + \mathrm{i}\omega\varepsilon(\mathbf{r}, \omega))\nabla u_\omega) = 0 & \text{in } \Omega \\ -(\sigma(\mathbf{r}, \omega) + \mathrm{i}\omega\varepsilon(\mathbf{r}, \omega))\nabla u_\omega \cdot \mathbf{n} = g & \text{on } \partial\Omega, \end{cases} \tag{1}$$

where σ and ε are the conductivity and permittivity, respectively, which depend on the position $\mathbf{r} = (x, y, z)$ and ω. Here, $\mathbf{n}$ is the outward unit normal vector on $\partial\Omega$ and g is the magnitude of the current density on $\partial\Omega$ due to the injection current. On current injection electrodes $\mathcal{E}_j$ and $\mathcal{E}_k$, we have $\int_{\mathcal{E}_j} g \, \mathrm{d}s = I = -\int_{\mathcal{E}_k} g \, \mathrm{d}s$ where $\mathrm{d}s$ is the surface element. The Neumann data g is zero on the regions of boundary not contacting with current injection electrodes. Setting a reference voltage having $\int_{\partial\Omega} u_\omega = 0$, we can obtain a unique solution u_ω of (1) from σ, ϵ and

g. Denoting real and imaginary parts of u_ω by $v_\omega = \mathrm{Re}\, u_\omega$ and $h_\omega = \mathrm{Im}\, u_\omega$, respectively, the boundary value problem in (1) can be expressed as the following coupled system:

$$\begin{cases} \nabla \cdot (\sigma \nabla v_\omega) - \nabla \cdot (\omega \varepsilon \nabla h_\omega) = 0 & \text{in } \Omega \\ \nabla \cdot (\omega \varepsilon \nabla v_\omega) + \nabla \cdot (\sigma \nabla h_\omega) = 0 & \text{in } \Omega \\ \mathbf{n} \cdot (-\sigma \nabla v_\omega + \omega \varepsilon \nabla h_\omega) = g & \text{on } \partial \Omega \\ \mathbf{n} \cdot (-\sigma \nabla h_\omega - \omega \varepsilon \nabla v_\omega) = 0 & \text{on } \partial \Omega. \end{cases} \tag{2}$$

We focus on a mathematical model for a 16-channel multi-frequency EIT system described by Oh *et al* (2007a, 2007b). Using the fdEIT system, we may inject currents with several different sinusoidal frequencies of $\omega_1, \omega_2, \ldots, \omega_m$, for example, 10 Hz $\leqslant \frac{\omega_1}{2\pi} \leqslant \frac{\omega_2}{2\pi} \leqslant \cdots \leqslant \frac{\omega_m}{2\pi} \leqslant$ 500 kHz. In this paper, we will express the induced boundary voltage as

$$f_\omega = u_\omega|_{\partial \Omega},$$

where u_ω is a solution of (1) or (2). As explained in the following sections, we will use a weighted frequency difference of the boundary voltage data

$$f_{\omega_k} - \alpha f_{\omega_l} \qquad \text{with} \qquad \omega_k \neq \omega_l$$

to reconstruct an image of a weighted frequency difference of complex conductivity values

$$\alpha[\sigma(\mathbf{r}, \omega_k) + \mathrm{i}\omega_k \varepsilon(\mathbf{r}, \omega_k)] - [\sigma(\mathbf{r}, \omega_l) + \mathrm{i}\omega_l \varepsilon(\mathbf{r}, \omega_l)],$$

where α is an appropriate constant.

Use of $f_{\omega_k} - \alpha f_{\omega_l}$ together with a complex sensitivity matrix is the key idea to minimize undesirable effects of modeling errors. It is important to understand how $\alpha[\sigma(\mathbf{r}, \omega_k) + \mathrm{i}\omega \varepsilon(\mathbf{r}, \omega_k)] - [\sigma(\mathbf{r}, \omega_l) + \mathrm{i}\omega \varepsilon(\mathbf{r}, \omega_l)]$ is related with $f_{\omega_k} - \alpha f_{\omega_l}$. In the following section, we investigate the sensitivity of $f_{\omega_k} - \alpha f_{\omega_l}$ to the presence of an anomaly. We will derive a representation formula providing a relation between boundary voltage data and change of complex conductivity across the anomaly.

2.2. Sensitivity analysis

We assume that the imaging object Ω is a circular saline tank that is treated as a unit disk and an anomaly D is located inside Ω. The complex conductivity distribution $\gamma(\mathbf{r}, \omega) = \sigma(\mathbf{r}, \omega) + \mathrm{i}\omega \varepsilon(\mathbf{r}, \omega)$ changes abruptly across the boundary of the anomaly, ∂D. We set

$$\sigma(\mathbf{r}, \omega) = \begin{cases} \sigma_b(\omega) & \text{if } \mathbf{r} \in \Omega \backslash \overline{D} \\ \sigma_a(\omega) & \text{if } \mathbf{r} \in D \end{cases} \qquad \text{and} \qquad \varepsilon(\mathbf{r}, \omega) = \begin{cases} \varepsilon_b(\omega) & \text{if } \mathbf{r} \in \Omega \backslash \overline{D} \\ \varepsilon_a(\omega) & \text{if } \mathbf{r} \in D. \end{cases} \tag{3}$$

The complex conductivities $\sigma_a + \mathrm{i}\omega \varepsilon_a$ and $\sigma_b + \mathrm{i}\omega \varepsilon_b$ are constants at each frequency ω but they may change with ω.

The following representation formula explains how $f_{\omega_2} - \alpha_b f_{\omega_1}$ is related with the anomaly D.

Lemma 2.1. *Under the assumption* (3)*, we have*

$$f_{\omega_2}(\mathbf{r}) - \alpha_b f_{\omega_1}(\mathbf{r}) = \int_D \frac{\mathbf{r} - \mathbf{r}'}{\pi |\mathbf{r} - \mathbf{r}'|^2} \cdot [\tau_2 \nabla u_{\omega_2}(\mathbf{r}') - \tau_1 \nabla u_{\omega_1}(\mathbf{r}')] \, \mathrm{d}\mathbf{r}', \qquad \mathbf{r} \in \partial \Omega, \tag{4}$$

where

$$\alpha_b = \frac{\sigma_b(\omega_1) + \mathrm{i}\omega_1 \varepsilon_b(\omega_1)}{\sigma_b(\omega_2) + \mathrm{i}\omega_2 \varepsilon_b(\omega_2)}$$

and

$$\tau_j = \frac{(\sigma_b(\omega_j) - \sigma_a(\omega_j)) + \mathrm{i}\omega_j (\varepsilon_b(\omega_j) - \varepsilon_a(\omega_j))}{\sigma_b(\omega_2) + \mathrm{i}\omega_2 \varepsilon_b(\omega_2)}, \qquad j = 1, 2.$$

Proof. Let $\mathbf{r} \in \partial\Omega$ and $\mathbf{r}_t = \mathbf{r} + t\mathbf{n}(\mathbf{r})$. Note that $\mathbf{r}_t \in \mathbb{R}^2 \setminus \Omega$ for $t > 0$. Denote $\Phi(\mathbf{r}, \mathbf{r}') = \frac{1}{2\pi} \log|\mathbf{r} - \mathbf{r}'|$, the fundamental solution of the Laplace equation. Since $\nabla^2\Phi(\mathbf{r}_t, \mathbf{r}') = 0$ for $\mathbf{r}' \in \Omega$ and $t > 0$, we have

$$0 = (\sigma_b(\omega) + i\omega\varepsilon_b(\omega)) \int_\Omega \nabla^2\Phi(\mathbf{r}_t, \mathbf{r}')u_\omega(\mathbf{r}')\,d\mathbf{r}', \quad \text{for } t > 0.$$

Integrating by parts, we get

$$\int_{\partial\Omega} g(\mathbf{r}')\Phi(\mathbf{r}_t, \mathbf{r}')\,ds_{\mathbf{r}'} + [\sigma_b(\omega) + i\omega\varepsilon_b(\omega)] \int_{\partial\Omega} \partial_\mathbf{n}\Phi(\mathbf{r}_t, \mathbf{r}')f_\omega(\mathbf{r}')\,ds_{\mathbf{r}'}$$
$$= ([\sigma_b(\omega) - \sigma_a(\omega)] + i\omega[\varepsilon_b(\omega) - \varepsilon_a(\omega)]) \int_D \nabla\Phi(\mathbf{r}_t, \mathbf{r}') \cdot \nabla u_\omega(\mathbf{r}')\,d\mathbf{r}', \quad (5)$$

where $\partial_\mathbf{n} = \mathbf{n} \cdot \nabla$ and $t > 0$. We choose two different frequencies of ω_1 and ω_2 and eliminate the integral term involving the input current g in (5). With $\omega_1 < \omega_2$, we have the following identity: for $\mathbf{r} \in \mathbb{R}^d \setminus \overline{\Omega}$,

$$\int_{\partial\Omega} \partial_\mathbf{n}\Phi(\mathbf{r}_t, \mathbf{r}')[f_{\omega_2}(\mathbf{r}') - \alpha_b f_{\omega_1}(\mathbf{r}')]\,ds_{\mathbf{r}'}$$
$$= \int_D \nabla\Phi(\mathbf{r}_t, \mathbf{r}') \cdot [\tau_2\nabla u_{\omega_2}(\mathbf{r}') - \tau_1\nabla u_{\omega_1}(\mathbf{r}')]\,d\mathbf{r}'. \quad (6)$$

It follows from the well-known trace formula for singular integral that

$$-\frac{1}{2}[f_{\omega_2}(\mathbf{r}') - \alpha_b f_{\omega_1}(\mathbf{r}')] = \lim_{t \to 0^+} \int_{\partial\Omega} \partial_\mathbf{n}\Phi(\mathbf{r} + t\mathbf{n}(\mathbf{r}), \mathbf{r}')[f_{\omega_2}(\mathbf{r}') - \alpha_b f_{\omega_1}(\mathbf{r}')]\,ds_{\mathbf{r}'} \quad (7)$$

for $\mathbf{r} \in \partial\Omega$. This completes the proof of (4) and it tells that real and imaginary parts of $f_{\omega_2} - \alpha_b f_{\omega_1}$ correspond to those of $\tau_2\nabla u_{\omega_2} - \tau_1\nabla u_{\omega_1}$ inside D, respectively. □

Observation 2.2. Average directions of $\nabla v_1, \nabla v_2, \nabla h_1, \nabla h_2$ on D are approximately parallel or anti-parallel provided that the injection current is a projection current (Isaacson 1986) and D is small,

$$\left| \int_D \nabla v_1(\mathbf{r})\,d\mathbf{r} \times \int_D \nabla v_2(\mathbf{r})\,d\mathbf{r} \right| \approx 0 \qquad \text{and} \qquad \left| \int_D \nabla v_j(\mathbf{r})\,d\mathbf{r} \times \int_D \nabla h_j(\mathbf{r})\,d\mathbf{r} \right| \approx 0$$

for $j = 1, 2$. Under these approximations, real and imaginary parts of (4) can be approximated by

$$\text{Re}\{f_{\omega_2}(\mathbf{r}) - \alpha_b f_{\omega_1}(\mathbf{r})\} \approx C_1\left(\omega_1, \omega_2, \frac{\sigma_a}{\sigma_b}, \frac{\varepsilon_a}{\varepsilon_b}\right) \int_D \frac{\mathbf{r} - \mathbf{r}'}{\pi|\mathbf{r} - \mathbf{r}'|^2} \cdot \nabla v_1(\mathbf{r}')\,d\mathbf{r}', \quad \mathbf{r} \in \partial\Omega$$
$$\text{Im}\{f_{\omega_2}(\mathbf{r}) - \alpha_b f_{\omega_1}(\mathbf{r})\} \approx C_2\left(\omega_1, \omega_2, \frac{\sigma_a}{\sigma_b}, \frac{\varepsilon_a}{\varepsilon_b}\right) \int_D \frac{\mathbf{r} - \mathbf{r}'}{\pi|\mathbf{r} - \mathbf{r}'|^2} \cdot \nabla v_1(\mathbf{r}')\,d\mathbf{r}', \quad \mathbf{r} \in \partial\Omega, \quad (8)$$

where C_1 and C_2 are constants depending on $\omega_1, \omega_2, \frac{\sigma_a}{\sigma_b}$ and $\frac{\varepsilon_a}{\varepsilon_b}$.

We will numerically verify this observation in section 3.1 (see figure 2). Although various numerical simulations support the observation 2.2 for a quite general anomaly D, we still do not have its theoretical justification which requires very technical analysis. Kwon *et al* (2002) and Ammari and Seo (2003) provided some analysis to estimate the direction of the vector $\int_D \nabla v_1(\mathbf{r})\,d\mathbf{r}$ when $\omega_1 = 0$.

Observation 2.3. As long as the complex conductivity value of the anomaly is different from that of the background, the weighted frequency-difference voltage in (4) contains information to detect the anomaly even for the case where $\sigma_l(\omega_1) = \sigma_l(\omega_2)$ and $\varepsilon_l(\omega_1) = \varepsilon_l(\omega_2)$ for $l = a, b$

(no change in conductivity and permittivity with respect to frequency for both anomaly and background). In this case, the formula for the imaginary part in (8) can be simplified as

$$\text{Im}\{f_{\omega_2}(\mathbf{r}_j) - \alpha_b f_{\omega_1}(\mathbf{r}_j)\} \approx |D| \left[\frac{\omega_2 \varepsilon_b}{\sigma_b} \left(\frac{\sigma_a}{\sigma_b} - \frac{\varepsilon_a}{\varepsilon_b} \right) \frac{(\mathbf{z} - \mathbf{r}_j) \cdot \nabla v_1(\mathbf{z})}{|\mathbf{z} - \mathbf{r}_j|^2} \right], \quad (9)$$

where $\mathbf{r}_j$ is the center of the electrode $\mathcal{E}_j$ for each $j = 1, \ldots, 16$ and $\mathbf{z}$ is the center of D. Hence, we can detect D provided that $\frac{\sigma_a}{\sigma_b} \neq \frac{\varepsilon_a}{\varepsilon_b}$.

We will numerically verify this observation in section 3.2 (see figure 3).

2.3. Frequency-difference image reconstruction algorithm

We assume a 16-channel multi-frequency EIT system (Oh *et al* 2007a, 2007b) where we sequentially inject 15 linearly independent sinusoidal currents $I \sin(\omega t)$ using adjacent pairs of electrodes $\mathcal{E}_j$ and $\mathcal{E}_{j+1}$ for $j = 1, 2, \ldots, 15$. Resulting complex voltage u_ω^j satisfies the following mixed boundary value problem:

$$\begin{cases} \nabla \cdot \left(\gamma_\omega \nabla u_\omega^j \right) = 0 & \text{in } \Omega \\ I = -\int_{\mathcal{E}_j} \gamma_\omega \frac{\partial u_\omega^j}{\partial \mathbf{n}} \, \mathrm{d}s = \int_{\mathcal{E}_{j+1}} \gamma_\omega \frac{\partial u_\omega^j}{\partial \mathbf{n}} \, \mathrm{d}s \\ \int_{\partial \Omega} u_\omega^j = 0, \quad \nabla u_\omega^j \times \mathbf{n}|_{\mathcal{E}_j} = 0 = \nabla u_\omega^j \times \mathbf{n}|_{\mathcal{E}_{j+1}} \\ \gamma_\omega \frac{\partial u_\omega^j}{\partial \mathbf{n}} = 0 & \text{on } \partial \Omega \setminus \overline{\mathcal{E}_j \cup \mathcal{E}_{j+1}}, \end{cases} \quad (10)$$

where $\frac{\partial u}{\partial \mathbf{n}} = \nabla u \cdot \mathbf{n}$. Primarily for the simplification, we use the simple electrode model which could be enough for an EIT system utilizing the four-electrode measurement method. One may adopt a more sophisticated electrode model such as the shunt model or complete electrode model (Cheng *et al* 1989).

We use two sets of measured boundary voltages $f_{\omega_1}^j(k) = u_{\omega_1}^j \big|_{\mathcal{E}_k}$ and $f_{\omega_2}^j(k) = u_{\omega_2}^j \big|_{\mathcal{E}_k}$ at different frequencies of ω_1 and ω_2, respectively. According to (8), it is desirable to use a weighted frequency-difference voltage data $f_{\omega_2}^j(k) - \alpha_b f_{\omega_1}^j(k)$. Assume that γ_{ω_1} and γ_{ω_2} have homogeneous backgrounds with complex conductivity values of $\hat{\gamma}_1$ and $\hat{\gamma}_2$, respectively, and $\gamma_{\omega_1} = \hat{\gamma}_1$ and $\gamma_{\omega_2} = \hat{\gamma}_2$ near $\partial \Omega$. In this case,

$$\alpha_b = \frac{\hat{\gamma}_1}{\hat{\gamma}_2} \qquad \text{and} \qquad \gamma_{\omega_1} - \alpha_b \gamma_{\omega_2} = 0 \quad \text{on } \partial \Omega.$$

Since the complex number α_b is not available in practice, we take α_b as a minimizer of the following sum:

$$\eta(\alpha) = \sum_k \sum_j \left| f_{\omega_2}^j(k) - \alpha f_{\omega_1}^j(k) \right|^2.$$

In fdEIT, we try to reconstruct an image of $\delta\gamma = \alpha_b \gamma_{\omega_2} - \gamma_{\omega_1}$ from $f_{\omega_2}^j - \alpha_b f_{\omega_1}^j$. We may use the *output least-square method* for the following misfit functional:

$$\Psi(\delta\gamma) = \sum_{j=1}^{15} \int_{\partial \Omega} \left| \delta U^j - \left(f_{\omega_2}^j - \alpha_b f_{\omega_1}^j \right) \right|^2 \, \mathrm{d}s, \quad (11)$$

where $\delta U^j = \delta u^j|_{\partial\Omega}$ is the boundary value of δu^j that is a solution of the following mixed boundary value problem:

$$\begin{cases} \nabla \cdot \left(\alpha_b^{-1}(\gamma_{\omega_1} + \delta\gamma)\nabla\delta u^j\right) = \nabla \cdot \left(\delta\gamma\nabla u_{\omega_1}^j\right) & \text{in } \Omega \\[2mm] 0 = \displaystyle\int_{\mathcal{E}_j} \gamma_{\omega_2} \frac{\partial\delta u^j}{\partial\mathbf{n}}\,\mathrm{d}s = \int_{\mathcal{E}_{j+1}} \gamma_{\omega_2} \frac{\partial\delta u^j}{\partial\mathbf{n}}\,\mathrm{d}s \\[2mm] \displaystyle\int_{\partial\Omega} \delta u^j = 0, \quad \nabla\delta u^j \times \mathbf{n}|_{\mathcal{E}_j} = 0 = \nabla\delta u^j \times \mathbf{n}|_{\mathcal{E}_{j+1}} \\[2mm] \gamma_{\omega_2} \dfrac{\partial\delta u^j}{\partial\mathbf{n}} = 0 & \text{on } \partial\Omega \setminus \overline{\mathcal{E}_j \cup \mathcal{E}_{j+1}}. \end{cases} \tag{12}$$

We can view δu^j as a nonlinear function of $\delta\gamma$, where δu^j corresponds to $u_{\omega_2}^j - \alpha_b u_{\omega_1}^j$. Applying integration by parts to the relation $\nabla \cdot \left(\delta\gamma\nabla u_{\omega_1}^j\right) = -\nabla \cdot \left(\alpha_b^{-1}(\gamma_{\omega_1} + \delta\gamma)\nabla\delta u^j\right)$ yields the following:

$$\int_\Omega \delta\gamma\nabla u_{\omega_1}^j \cdot \nabla u_{\omega_2}^k\,\mathrm{d}\mathbf{r} - \int_{\partial\Omega} \delta\gamma\frac{\partial\left(u_{\omega_1}^j\right)}{\partial\mathbf{n}} u_{\omega_2}^k\,\mathrm{d}s$$

$$= -\int_\Omega \gamma_{\omega_2}\nabla\delta u^j \cdot \nabla u_{\omega_2}^k\,\mathrm{d}\mathbf{r} + \int_{\partial\Omega} \gamma_{\omega_2}\frac{\partial(\delta U^j)}{\partial\mathbf{n}} u_{\omega_2}^k\,\mathrm{d}s$$

$$= \int_\Omega \nabla \cdot \left(\gamma_{\omega_2}\nabla u_{\omega_2}^k\right)\delta u^j\,\mathrm{d}\mathbf{r} - \int_{\partial\Omega} \gamma_{\omega_2}\frac{\partial\left(u_{\omega_2}^k\right)}{\partial\mathbf{n}}\delta u^j\,\mathrm{d}s.$$

Note that $\delta\gamma = 0$ on $\partial\Omega$ and $\nabla \cdot \left(\gamma_{\omega_2}\nabla u_{\omega_2}^k\right) = 0$ in Ω. We obtain

$$\int_\Omega \delta\gamma\nabla u_{\omega_1}^j \cdot \nabla u_{\omega_2}^k\,\mathrm{d}\mathbf{r} = \int_{\partial\Omega} \delta U^j g^k\,\mathrm{d}s \tag{13}$$

for each $j, k = 1, 2, 3, \ldots, 15$ where g^k is the Neumann data corresponding to $u_{\omega_2}^k$.

It is equivalent to

$$\int_\Omega \left(\alpha_b\gamma_{\omega_2} - \gamma_{\omega_1}\right)\nabla u_{\omega_1}^j \cdot \nabla u_{\omega_2}^k\,\mathrm{d}\mathbf{r} = \int_{\partial\Omega} \left(f_{\omega_2}^j - \alpha_b f_{\omega_1}^j\right)g^k\,\mathrm{d}s \tag{14}$$

for each $j, k = 1, 2, 3, \ldots, 15$. Let $\hat{u}_l^j$, $l = 1, 2$, be solutions of (10) with $\hat{\gamma}_l$ in place of γ_ω. We replace the terms $u_{\omega_1}^j$ and $u_{\omega_2}^k$ in the left integrand of (13) by $\hat{u}_1^j$ and $\hat{u}_2^k$, respectively, and then (13) can be approximated by

$$\int_\Omega \left(\alpha_b\gamma_{\omega_2} - \gamma_{\omega_1}\right)\nabla\hat{u}_1^j \cdot \nabla\hat{u}_2^k\,\mathrm{d}\mathbf{r} \approx \int_{\partial\Omega} \left(f_{\omega_2}^j - \alpha_b f_{\omega_1}^j\right)g^k\,\mathrm{d}s. \tag{15}$$

Since $\hat{\gamma}_l\hat{u}_l^j = \hat{u}_0^j$ where $\hat{u}_0^j$ is a solution of (10) with $\gamma_\omega = 1$, (15) becomes

$$\int_\Omega \left(\alpha_b\gamma_{\omega_2} - \gamma_{\omega_1}\right)\nabla\left(\frac{\hat{u}_0^j}{\hat{\gamma}_1}\right) \cdot \nabla\left(\frac{\hat{u}_0^k}{\hat{\gamma}_2}\right)\mathrm{d}\mathbf{r} \approx \int_{\partial\Omega} \left(f_{\omega_2}^j - \alpha_b f_{\omega_1}^j\right)g^k\,\mathrm{d}s. \tag{16}$$

Writing $\delta\gamma = \alpha_b\gamma_{\omega_2} - \gamma_{\omega_1}$, the normalized change of complex conductivity from ω_1 to ω_2 is computed from

$$\int_\Omega \delta\gamma\nabla\left(\frac{\hat{u}_0^j}{\hat{\gamma}_1}\right) \cdot \nabla\left(\frac{\hat{u}_0^k}{\hat{\gamma}_2}\right)\mathrm{d}\mathbf{r} \approx \left(f_{\omega_2}^j(k) - \alpha_b f_{\omega_1}^j(k)\right)I \tag{17}$$

for $j, k = 1, 2, 3, \ldots, 15$. The number of degrees of freedom N is limited to the number of independent voltage measurements in such a way that $N \leqslant \frac{16 \times 15}{2}$. We decompose the imaging domain Ω into $\Omega = \cup_{i=1}^N \Omega_i$ where Ω_i is the ith pixel. Let χ_{Ω_i} be the characteristic function of

the *i*th element Ω_i. Assuming a frequency-difference conductivity $\delta\gamma = \sum_{i=1}^{N} \delta\gamma_i \chi_{\Omega_i}$, (17) can be reduced to the following linear system:

$$\sum_{i=1}^{N} \left[\frac{1}{I} \int_{\Omega_i} \nabla \left(\frac{\hat{u}_0^j}{\hat{\gamma}_1} \right) \cdot \nabla \left(\frac{\hat{u}_0^k}{\hat{\gamma}_2} \right) d\mathbf{r} \right] \delta\gamma_i \approx f_{\omega_2}^j(k) - \alpha_b f_{\omega_1}^j(k) \tag{18}$$

for $j, k = 1, 2, 3, \ldots, 15$. This system can be expressed in a matrix form as

$$\frac{1}{I \hat{\gamma}_1 \hat{\gamma}_2} [\mathbb{A}] \vec{\delta\gamma} \approx \vec{f}_{\omega_1} - \alpha_b \vec{f}_{\omega_2}, \tag{19}$$

where $\vec{\delta\gamma} = [\delta\gamma_1, \ldots, \delta\gamma_N]^T$ and the *mn*th entry of $\mathbb{A}$ is $a_{mn} = \int_{\Omega_n} \nabla \hat{u}_0^j \cdot \nabla \hat{u}_0^k d\mathbf{r}$ with $m = 15(j-1) + k$. Frequency-difference image reconstruction can be performed by solving (19) for $\vec{\delta\gamma}$. Note that the sensitivity matrix $\mathbb{A}$ is complex and the use of complex numbers, $\hat{\gamma}_1$, $\hat{\gamma}_2$ and α_b in (19) is important.

2.4. Numerical simulation

We performed numerical simulations on a unit disk $\Omega = \{(x, y) : x^2 + y^2 \leqslant 1\}$ with 16 electrodes equally spaced around its circumference. We generated a finite element mesh of the disk using 1038 triangular elements and 552 nodes. We assumed that the disk was filled with a saline. Inside the disk, we placed an anomaly occupying the region $D = \{(x, y) : (x - 0.45)^2 + y^2 \leqslant 0.25^2\}$. Complex conductivity values of the saline and anomaly were chosen as shown in table 1 (Oh *et al* 2008). We used the PDE toolbox supported by Matlab (The Mathworks Inc., USA) and all computations were performed using a PC with a Pentium IV processor, 1GB RAM and Windows XP operating system.

We numerically solved the forward problem in (10) to generate simulated voltage data, $f_{\omega_1}^j$ and $f_{\omega_2}^j$ for $j = 1, \ldots, 15$. Frequency-difference image reconstructions of $\vec{\delta\gamma}$ were performed based on (19) where we used the set of weighted frequency-difference voltages $f_{\omega_2}^j(k) - \alpha_b f_{\omega_1}^j(k)$. The complex sensitivity matrix $\mathbb{A}$ was computed by using the corresponding forward solutions in the absence of the anomaly. For the frequency-difference image reconstructions, we used a separate mesh with a smaller number of triangular elements. Reconstructed images were displayed on a 30×30 square mesh by using a proper mapping and smoothing function.

3. Results

3.1. Numerical forward solution and verification of observation 2.2

Using the finite element method, we solved the forward problem in (10) at different frequencies varying from 100 Hz to 500 kHz. Figure 1 shows a numerical solution u_ω of (10) at 100 kHz for an injection current between a pair of neighboring electrodes. In order to numerically verify the observation 2.2, we used a projection current of a sinusoidal pattern (Isaacson 1986). The amplitude of the injection current at the *k*th electrode was chosen as $-\sin\left(\frac{\pi}{8}k + \frac{\pi}{4}\right)$. Figure 2 illustrates numerical solutions of (10) at 50, 100, 250 and 500 kHz supporting the observation 2.2.

3.2. Verification of observation 2.2

We tested the observation 2.2 using the proposed fdEIT algorithm. In figure 3, we assumed a model with a homogeneous background with $\sigma_b = 0.036$ S m^{-1} and $\varepsilon_b = 1.9 \times 10^{-9}$ F m^{-1}.
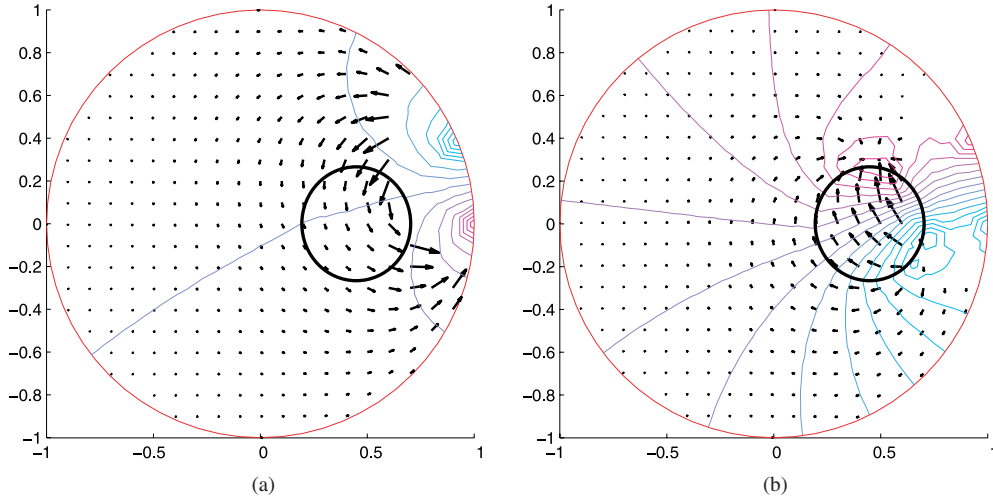
Figure 1. Equipotential lines (solid lines) and electric field streamlines (arrows) of the complex potential u_ω in (10) at $\omega/2\pi = 100$ kHz subject to an injection current between an adjacent pair of electrodes. Complex conductivity values of the anomaly and the background were those of the banana and the saline, respectively, in table 1. (a) Real part ($\mathrm{Re}\{u_\omega\}$) and (b) imaginary part ($\mathrm{Im}\{u_\omega\}$).

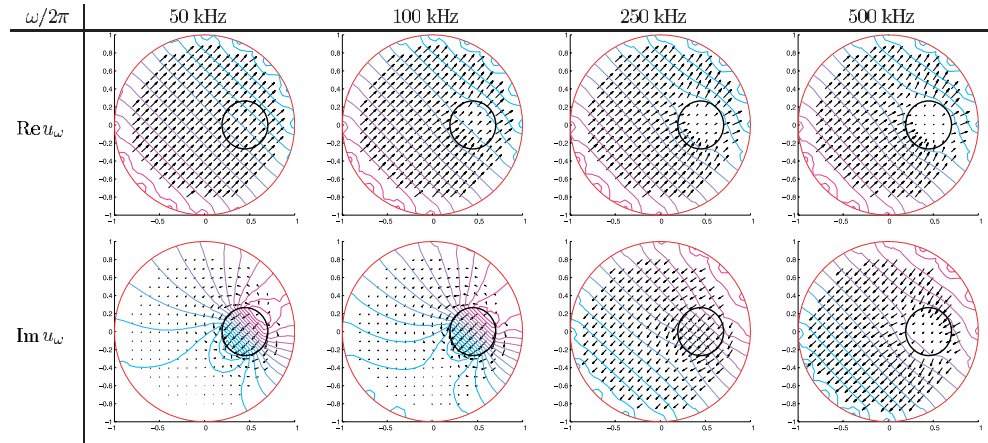**Figure 2.** Equipotential lines (solid lines) and electric field streamlines (arrows) of the complex potential u_ω at 50, 100, 250 and 500 kHz. Complex conductivity values of the anomaly and the background were the values of the banana and the saline, respectively, in table 1. The injection current was a projection current (Isaacson 1986), that is, the amplitude of the injection current at the kth electrode was $-\sin(\frac{\pi}{8}k + \frac{\pi}{4})$.

The circular anomaly had a conductivity $\sigma_a = 0.042$ S m^{-1}. Permittivity of the anomaly was chosen either as $\varepsilon_a = 9.7 \times 10^{-9}$ or 2.2×10^{-9} F m^{-1}. In the latter case, we had the condition of $\frac{\sigma_a}{\sigma_b} = \frac{\varepsilon_a}{\varepsilon_b}$. We used the same complex conductivity values for both ω_1 and ω_2 meaning that they had no frequency dependence. Reconstructed real- and imaginary-part of frequency-difference images in the middle of figure 3 clearly show that the anomaly D is visible provided that $\frac{\sigma_a}{\sigma_b} \neq \frac{\varepsilon_a}{\varepsilon_b}$. As shown in the rightmost image in figure 3, the proposed fdEIT algorithm is blind to the presence of D when $\frac{\sigma_a}{\sigma_b} = \frac{\varepsilon_a}{\varepsilon_b}$.

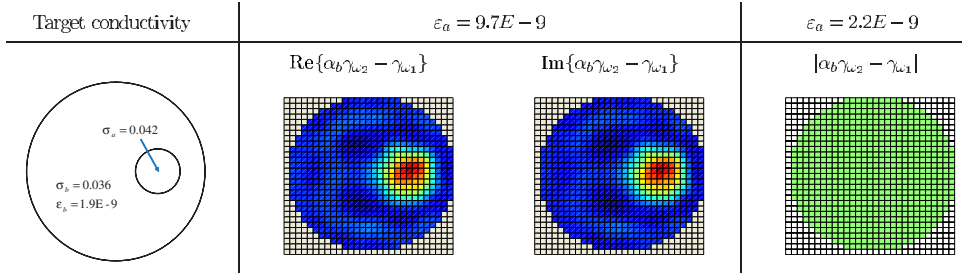| Target conductivity	$\varepsilon_a = 9.7E - 9$		$\varepsilon_a = 2.2E - 9$
	$\mathrm{Re}\{\alpha_b\gamma_{\omega_2} - \gamma_{\omega_1}\}$	$\mathrm{Im}\{\alpha_b\gamma_{\omega_2} - \gamma_{\omega_1}\}$	$|\alpha_b\gamma_{\omega_2} - \gamma_{\omega_1}|$

Figure 3. Reconstructed fdEIT images of the case where $\sigma(\omega_1) = \sigma(\omega_2)$ and $\varepsilon(\omega_1) = \varepsilon(\omega_2)$ for $\frac{\omega_1}{2\pi}$=1 kHz and $\frac{\omega_2}{2\pi}$=100 kHz. Two images in the middle show that the anomaly is still visible as long as $\frac{\sigma_a}{\sigma_b} \neq \frac{\varepsilon_a}{\varepsilon_b}$. The image on the right shows that fdEIT is blind to the anomaly when $\frac{\sigma_a}{\sigma_b} = \frac{\varepsilon_a}{\varepsilon_b}$.
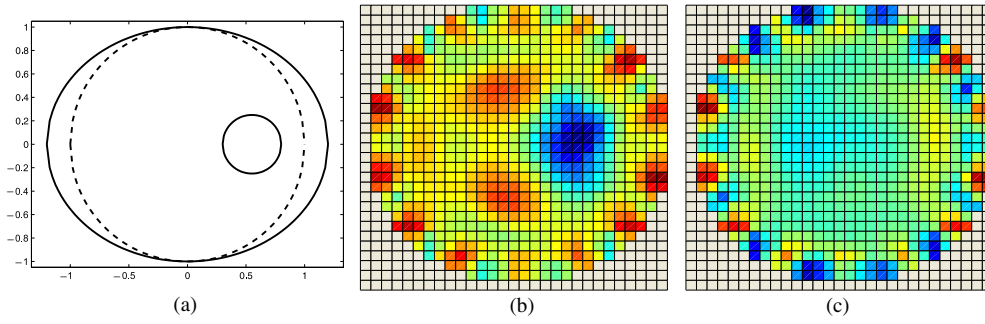

Figure 4. Effect of a boundary geometry error. (a) The ellipse with solid line was the true imaging domain and the circle in dashed line was the computational model domain. The small disk inside the domain was an anomaly. Complex conductivity values of the anomaly and the background were those of the banana and the saline in table 1, respectively. (b) and (c) are reconstructed static images (real-part images) at frequencies $\frac{\omega_1}{2\pi} = 100$ Hz and $\frac{\omega_2}{2\pi} = 50$ kHz, respectively. Each image was reconstructed using the boundary voltage data from the homogeneous computational model domain as the reference data.

3.3. Robustness against boundary geometry error

We tested the robustness of the fdEIT algorithm against a boundary geometry error. Let $\Omega_{\mathrm{true}} := \left\{(x, y) : \left(\frac{x}{1.2}\right)^2 + y^2 < 1\right\}$, an ellipse, be the true imaging domain and let the computational domain be the unit disk $\Omega_{\mathrm{comp}} := \{(x, y) : x^2 + y^2 < 1\}$ as in figure 4(a). We injected currents into the ellipsoidal imaging domain with a given true complex conductivity distribution at two different frequencies of $\frac{\omega_1}{2\pi} = 100$ Hz and $\frac{\omega_2}{2\pi} = 50$ kHz and computed two sets of simulated boundary voltages, $f_{\omega_1}^j$ and $f_{\omega_2}^j$ for $j = 1, \ldots, 15$, respectively. We injected the same currents into the circular homogeneous computational domain and computed two sets of boundary voltage data, $\tilde{f}_{\omega_1}^j$ and $\tilde{f}_{\omega_2}^j$ at ω_1 and ω_2, respectively. We computed the sensitivity matrix from the circular homogeneous computational domain that contains the modeling error.

There exist numerous static image reconstruction algorithms and the quality of a reconstructed image depends on a chosen algorithm. Since the primary purpose was to test the robustness of the fdEIT algorithm, we tried to avoid the issue on the choice of the static imaging algorithm. The fdEIT algorithm in (19) is proposed as a single-step algorithm based
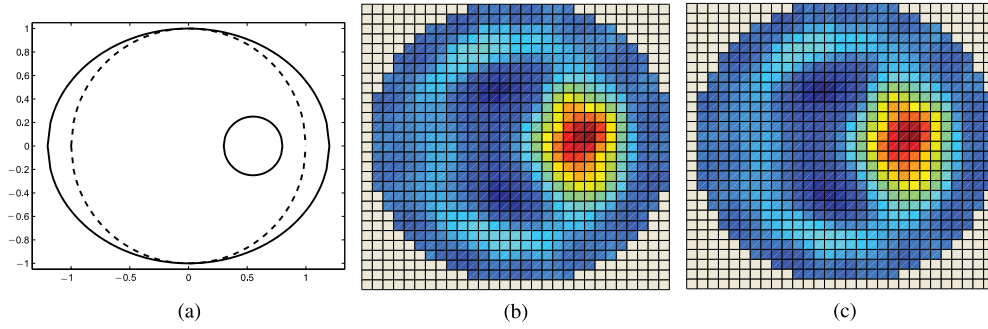
Figure 5. Robustness of the proposed fdEIT algorithm against a boundary geometry error. (a) The same true and computation domains explained in figure 4(a). (b) Real part of the reconstructed frequency-difference image $\text{Re}\{\alpha_b\gamma_{\omega_2} - \gamma_{\omega_1}\}$ and (c) imaginary-part image $\text{Im}\{\alpha_b\gamma_{\omega_2} - \gamma_{\omega_1}\}$. Two frequencies were $\frac{\omega_1}{2\pi} = 100$ Hz and $\frac{\omega_2}{2\pi} = 50$ kHz. The homogeneous computational model domain was used to compute the sensitivity matrix.

on the sensitivity matrix. For the purpose of comparison, we used a single-step truncated singular value decomposition method as a kind of static image reconstruction method.

First, we performed a static EIT image reconstruction at each frequency of ω_1 and ω_2 separately. Images in figure 4(b) and (c) using $f_{\omega_1}^j - \tilde{f}_{\omega_1}^j$ and $f_{\omega_2}^j - \tilde{f}_{\omega_2}^j$, respectively, can be considered as static images for the purpose of comparison with the fdEIT algorithm. Note that $\tilde{f}_{\omega_1}^j$ and $\tilde{f}_{\omega_2}^j$ contained the boundary geometry error and these static images show that its effect is quite severe. Second, we applied the simulated data $f_{\omega_2}^j - f_{\omega_1}^j$ to the fdEIT algorithm without using $\tilde{f}_{\omega_1}^j$ and $\tilde{f}_{\omega_2}^j$. Reconstructed frequency-difference images in figure 5(b) and (c) clearly show that the proposed fdEIT method is more robust against the boundary geometry error.

3.4. Simulation of frequency-difference imaging experiments

To see effects of complex numbers α_b, $\hat{\gamma}_1$ and $\hat{\gamma}_2$ in (19), we tried frequency-difference image reconstructions twice with and without using them. In all simulations, we fixed one reference frequency of $\omega_1/2\pi = 100$ Hz and chose four different higher frequencies of $\omega_2/2\pi = 50, 100, 250$ and 500 kHz.

Figure 6 shows the performance of the proposed fdEIT algorithm to reconstruct frequency-difference images the banana in the saline background. According to table 1, conductivities and permittivities of the banana at ω_2 were set to be much greater than those at ω_1 (100 Hz). These large differences between two chosen frequencies made the banana object very well distinguished in reconstructed frequency-difference images. For the cucumber object in the saline background, we could obtain similar results.

Figure 7 shows results for the PAA object in the saline background. Based on table 1, we set the conductivity of the PAA object to be almost constant for all chosen frequencies. Also, its permittivity value was significantly smaller than that of the banana with only a small frequency dependence. In figure 7, we can still recognize the PAA object supporting the observation 2.3 since the condition $\frac{\sigma_a}{\sigma_b} \neq \frac{\varepsilon_a}{\varepsilon_b}$ was met. For non-biological objects such as agar, AHG and TX151 listed in table 1, we could obtain similar results.

In all images of figures 6 and 7, we can see that uses of $\hat{\gamma}_1$, $\hat{\gamma}_2$ and α_b significantly enhance the image quality. This was more evident for imaginary-part images and also for the cases of $\omega_2/2\pi = 250$ and 500 kHz.

Table 1. Complex conductivity ($\sigma + i\omega\varepsilon$) values of seven different materials at five different frequencies used in numerical simulations. Saline was used as the background and others were used as anomalies. Complex conductivity values of the cucumber and banana mimic those of biological tissues. The rest of them including TX151, PAA, AHG and agar were used as non-biological objects. Oh *et al* (2008) explained the recipe to fabricate these objects and reported measured complex conductivity values summarized here.

Frequency (Hz)	σ (S m^{-1})						
	TX151	PAA	AHG	Agar	Cucumber	Banana	Saline
100	1.53×10^{-1}	1.83×10^{-1}	5.80×10^{-2}	9.30×10^{-2}	4.30×10^{-2}	7.00×10^{-3}	3.60×10^{-2}
50 000	1.51×10^{-1}	1.77×10^{-1}	5.80×10^{-2}	9.20×10^{-2}	1.05×10^{-1}	2.50×10^{-2}	3.60×10^{-2}
100 000	1.49×10^{-1}	1.77×10^{-1}	5.70×10^{-2}	9.10×10^{-2}	1.65×10^{-1}	4.20×10^{-2}	3.60×10^{-2}
250 000	1.49×10^{-1}	1.76×10^{-1}	5.50×10^{-2}	8.80×10^{-2}	3.13×10^{-1}	1.15×10^{-1}	3.30×10^{-2}
500 000	1.44×10^{-1}	1.70×10^{-1}	5.00×10^{-2}	8.30×10^{-2}	4.05×10^{-1}	3.61×10^{-1}	3.00×10^{-2}
	$\omega\epsilon$ (S m^{-1})						
100	0	0	0	0	1.46×10^{-6}	2.28×10^{-6}	0
50 000	5.17×10^{-4}	5.17×10^{-4}	6.26×10^{-4}	5.23×10^{-4}	7.59×10^{-2}	3.32×10^{-2}	5.94×10^{-4}
100 000	1.19×10^{-3}	1.19×10^{-3}	1.08×10^{-3}	8.47×10^{-4}	1.21×10^{-1}	6.07×10^{-2}	1.21×10^{-3}
250 000	3.18×10^{-3}	3.18×10^{-3}	3.15×10^{-3}	2.65×10^{-3}	1.92×10^{-1}	1.35×10^{-1}	3.96×10^{-3}
500 000	7.24×10^{-3}	7.24×10^{-4}	8.72×10^{-3}	8.24×10^{-3}	2.21×10^{-1}	2.58×10^{-1}	8.86×10^{-3}

Real-part image, $\mathrm{Re}(\alpha_b\gamma_{\omega_2} - \gamma_{\omega_1})$ of banana/saline

$\omega_2/2\pi$	50 kHz	100 kHz	250 kHz	500 kHz	
Target difference image					
fdEIT image using correct values of $\alpha_b, \hat{\gamma}_1, \hat{\gamma}_2$					
fdEIT image using $\alpha_b = \hat{\gamma}_1 = \hat{\gamma}_2 = 1$					

Imaginary-part image, $\mathrm{Im}(\alpha_b\gamma_{\omega_2} - \gamma_{\omega_1})$ of banana/saline

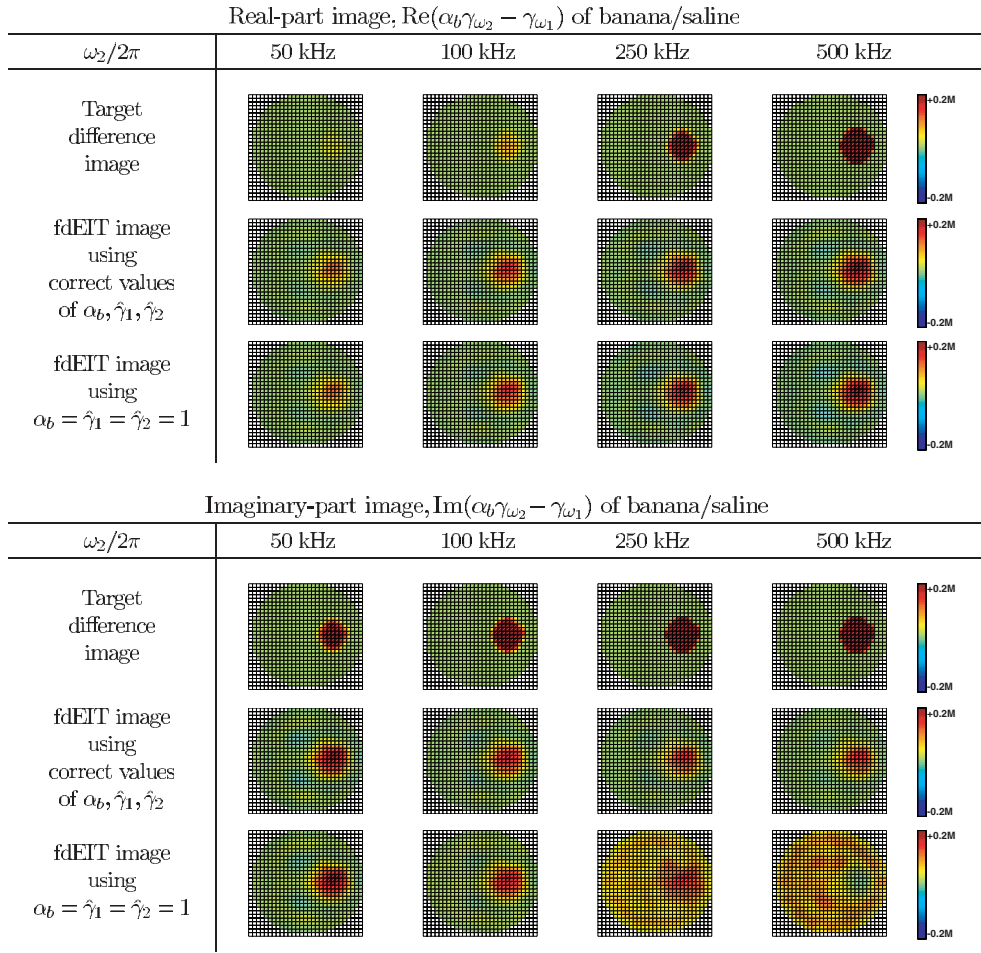| $\omega_2/2\pi$	50 kHz	100 kHz	250 kHz	500 kHz	
Target difference image					
fdEIT image using correct values of $\alpha_b, \hat{\gamma}_1, \hat{\gamma}_2$					
fdEIT image using $\alpha_b = \hat{\gamma}_1 = \hat{\gamma}_2 = 1$					

Figure 6. Reconstructed frequency-difference images of the banana placed in the saline background using $\omega_1/2\pi = 100$ Hz.

4. Discussion

Except for the extremely rare case of $\frac{\sigma_a}{\sigma_b} = \frac{\varepsilon_a}{\varepsilon_b}$, the proposed fdEIT algorithm can visualize an anomaly in reconstructed frequency-difference images. The contrast in a frequency-difference image stems from two factors. The first is a frequency dependence of a complex conductivity distribution to be imaged and the second is a contrast in complex conductivity values between an anomaly and background. This fdEIT method is robust against modeling errors and, therefore, will be advantageous in imaging a complex conductivity distribution inside the human body with an irregular boundary shape.

Though the fdEIT algorithm has a potential to overcome technical drawbacks of the conventional static EIT imaging method, we do not argue that it is free from the ill-posedness of the EIT image reconstruction problem. The ill-posedness is the inherent nature of the problem limiting the spatial resolution of a reconstructed image. The results in section 3.3 are promising but we need to further investigate how the boundary geometry error affects
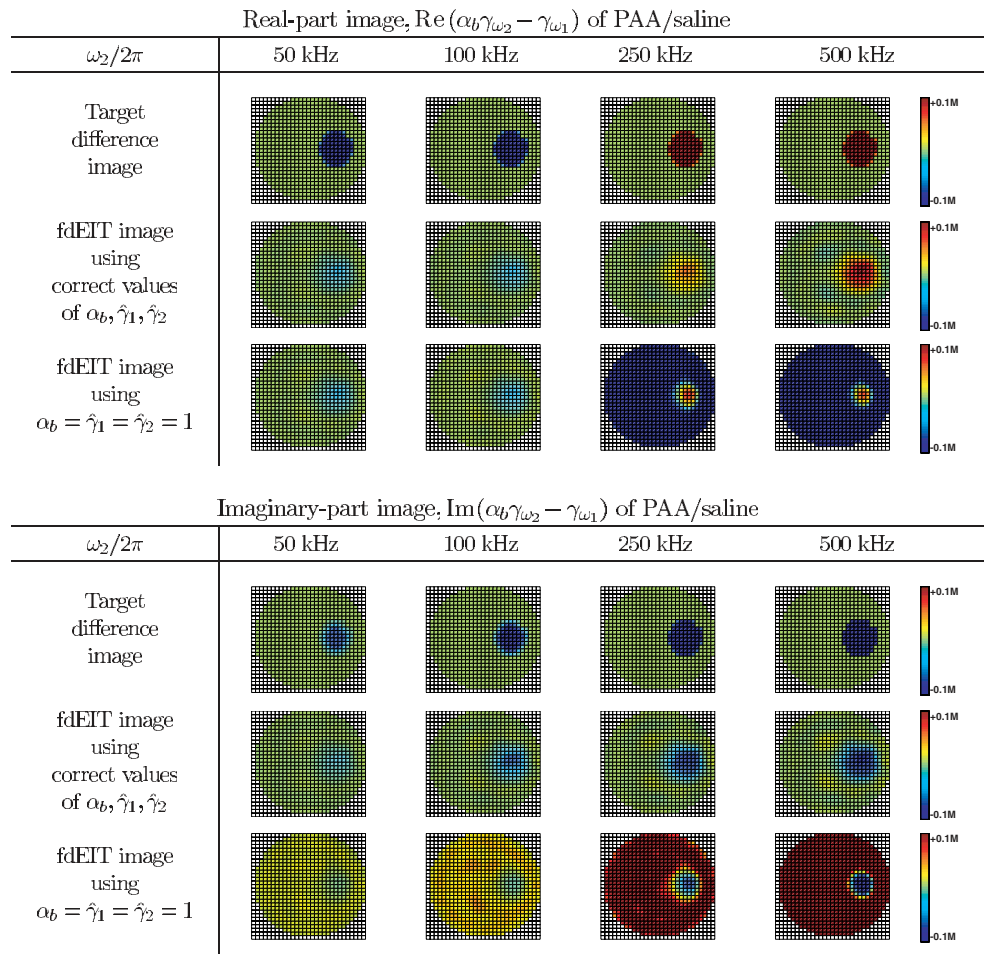
Real-part image, $\mathrm{Re}\,(\alpha_b\gamma_{\omega_2} - \gamma_{\omega_1})$ of PAA/saline

$\omega_2/2\pi$	50 kHz	100 kHz	250 kHz	500 kHz
Target difference image				
fdEIT image using correct values of $\alpha_b, \hat{\gamma}_1, \hat{\gamma}_2$				
fdEIT image using $\alpha_b = \hat{\gamma}_1 = \hat{\gamma}_2 = 1$				

Imaginary-part image, $\mathrm{Im}(\alpha_b\gamma_{\omega_2} - \gamma_{\omega_1})$ of PAA/saline

$\omega_2/2\pi$	50 kHz	100 kHz	250 kHz	500 kHz
Target difference image				
fdEIT image using correct values of $\alpha_b, \hat{\gamma}_1, \hat{\gamma}_2$				
fdEIT image using $\alpha_b = \hat{\gamma}_1 = \hat{\gamma}_2 = 1$				

Figure 7. Reconstructed frequency-difference images of the PAA object placed in the saline background using $\omega_1/2\pi = 100$ Hz.

the reconstructed frequency-difference image in our future study. Recent application studies show that EIT images with a low spatial resolution can be used in numerous clinical settings (Holder 2005). To improve their applicability, there should be improvements in consistency and accuracy of reconstructed images as well as efficient human interface methods.

Starting from the improved idea of the fdEIT method described in this paper, there must be future studies to advance it to the stage of clinical applications. Most of all, experimental validations must be followed by using two- and three-dimensional phantoms including biological materials of known complex conductivity spectra. In our future experimental studies, we can estimate $\hat{\gamma}_1$ and $\hat{\gamma}_2$ as the equivalent homogeneous complex conductivity values of the imaging object at frequencies ω_1 and ω_2, respectively. This can be done by using the measured boundary voltage data at each frequency. The weighting parameter α_b is a complex number in general and will be computed as $\alpha_b = \frac{\hat{\gamma}_1}{\hat{\gamma}_2}$. Its value mainly reflects the change of the equivalent homogeneous complex conductivity value of the imaging object with respect to the frequency change from ω_1 to ω_2.

In terms of the algorithm, we must investigate different kinds of regularization and numerical implementation techniques of the image reconstruction algorithm. We need to study the feasibility of an iterative algorithm where the complex sensitivity matrix is updated in each iteration. Effects of electrode contact impedance must be investigated since they can change with frequency. It will be worthwhile to try different kinds of electrode models. Theoretical advance is also needed since there is little knowledge on the forward and inverse problem governed by complex partial differential equations in (1) and (2). Frequency-difference detection rather than imaging is worth pursuing in some applications such as breast cancer detection.

5. Conclusion

Suggesting a frequency-difference image reconstruction algorithm properly handling the interplay of conductivity and permittivity, we showed the feasibility of frequency-difference EIT imaging. Numerical simulations showed that the complex parameters of $\hat{\gamma}_1$, $\hat{\gamma}_2$ and α_b play an important role in improving the image quality. The major advantage of frequency-difference EIT over static EIT is that it will be possible to reduce undesirable effects of modeling errors.

We plan to undertake experimental validation studies using saline tanks containing numerous anomalies with known complex conductivity spectra. We expect that frequency-difference EIT will be useful for clinical applications not supported by time-difference imaging. Even for the cases where time-difference imaging is applicable, frequency-difference imaging will be able to provide additional diagnostic information. We speculate that the future EIT system should be equipped with a multi-frequency capability producing spectroscopic time- and also frequency-difference images of an internal complex conductivity distribution.

References

Adler A and Lionheart W 2006 Uses and abuses of eidors: an extensible software base for EIT *Physiol. Meas.* **27** S25–42

Ammari H and Seo J K 2003 An accurate formula for the reconstruction of conductivity inhomogeneity *Adv. Appl. Math.* **30** 679–705

Cheney M, Isaacson D and Newell J C 1999 Electrical impedance tomography *SIAM Rev.* **41** 85–101

Cheng K S, Isaacson D, Newell J C and Gisser D G 1989 Electrode models for electric current computed tomography *IEEE Trans. Biomed. Eng.* **36** 918–24

Cheney M, Isaacson D, Newell J C, Simske S and Goble J 1990 NOSER: an algorithm for solving the inverse conductivity problem *Int. J. Imag. Syst. Tech.* **2** 66–75

Cheney M, Isaacson D, Somersalo E J, Isaacson E L and Coffey E J 1991 A layer-stripping reconstruction algorithm for impedance imaging *Proc. Ann. Int. Conf. IEEE EMBS* **13** 3–4

Gabriel S, Lau R W and Gabriel C 1996 The dielectric properties of biological tissues: II. Measurements in the frequency range 10 Hz to 20 GHz *Phys. Med. Biol.* **41** 2251–69

Geddes L A and Baker L E 1967 The specific resistance of biological material: a compendium of data for the biomedical engineer and physiologist *Med. Biol. Eng.* **5** 271–93

Griffiths H and Ahmed A 1987 A dual-frequency applied potential tomography technique: computer simulations *Clin. Phys. Physiol. Meas.* **8** 103–7

Grimnes S and Martinsen O G 2000 *Bioimpedance and Bioelectricity Basics* (London: Academic)

Holder D 2005 *Electrical Impedance Tomography: Methods, History and Applications* (Bristol: Institute of Physics Publishing)

Isaacson D 1986 Distinguishability of conductivities by electric current computed tomography *IEEE Trans. Med. Imag.* **5** 92–5

Isaacson D, Mueller J L, Newell J C and Siltanen S 2004 Reconstructions of chest phantoms by the d-bar method for electrical impedance tomography *IEEE Trans. Biomed. Eng.* **23** 821–8

Jam H, Isaacson D, Edic P M and Newell J C 1997 Electrical impedance tomography of complex conductivity distributions with noncircular boundary *IEEE Trans. Biomed. Eng.* **44** 1051–60

Kwon O, Seo J K and Yoon J R 2002 A real-time algorithm for the location search of discontinuous conductivities with one measurement *Comm. Pure Appl. Math.* **55** 1–29

Lionheart W, Polydorides N and Borsic A 2005 The reconstruction problem *Electrical Impedance Tomography: Methods, History and Applications* ed D S Holder (Bristol: Institute of Physics Publishing)

Metherall P, Barber D C, Smallwood R H and Brown B H 1996 Three-dimensional electrical impedance tomography *Nature* **380** 509–12

Oh T I, Koo W, Lee K H, Kim S M, Lee J, Kim S W, Seo J K and Woo E J 2008 Validation of a multi-frequency electrical impedance tomography (mfEIT) system KHU Mark1: impedance spectroscopy and time-difference imaging *Physiol. Meas.* **29** 295–307

Oh T I, Lee K H, Kim S M, Koo W, Woo E J and Holder D 2007b Calibration methods for a multi-channel multi-frequency EIT system *Physiol. Meas.* **28** 1175–88

Oh T I, Woo E J and Holder D 2007a Multi-frequency EIT system with radially symmetric architecture: KHU Mark1 *Physiol. Meas.* **28** S183–96

Saulnier G J, Blue J C, Newell J C, Isaacson D and Edic P M 2001 Electrical impedance tomography *IEEE Signal Proc. Mag.* **18** 31–43

Scalfe J M, Tozer R C and Freeston I L 1994 Conductivity and permittivity images from an induced current electrical impedance tomography system *IEE Proc. Sci. Meas. Technol.* **141** 356–62

Schlappa J, Annese E and Griffiths H 2000 Systematic errors in multi-frequency EIT *Physiol. Meas.* **21** 111–8

Webster J G 1990 *Electrical Impedance Tomography* (Bristol: Hilger)

Woo E J, Hua P, Webster J G and Tompkins W J 1993 A robust image reconstruction algorithm and its parallel implementation in electrical impedance tomography *IEEE Trans. Med. Imag.* **12** 137–46

Yerworth R J, Bayford R H, Brown B, Milnes P, Conway M and Holder D S 2003 Electrical impedance tomography spectroscopy (EITS) for human head imaging *Physiol. Meas.* **24** 477–89

Yorkey T J, Webster J G and Tompkins W J 1987 Comparing reconstruction algorithms for electrical impedance tomography *IEEE Trans. Biomed. Eng.* **BME-34** 843–52